

pubs.acs.org/acsaom Article

Thermal-Strain-Enabled Enhanced Emission from UV Laser-Induced Defect Levels near the Surface of Multilayer MoS₂

3 Sinto Varghese, Noah Hurley, Steve Kamau, Yan Jiang, Roberto Gonzalez Rodriguez, Bhojraj Bhandari,

⁴ Tengteng Lyu, Hao Yan, Yuanxi Wang, Anupama B. Kaul, Jingbiao Cui, and Yuankun Lin*



Cite This: https://doi.org/10.1021/acsaom.4c00276



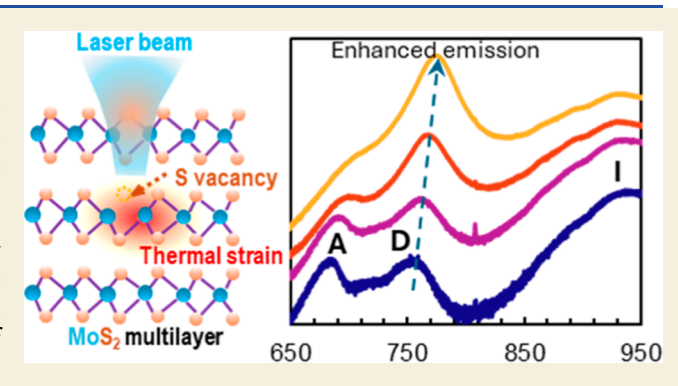
ACCESS

III Metrics & More

Article Recommendations

sı Supporting Information

s ABSTRACT: Monolayer two-dimensional (2D) materials have 6 been intensively studied, while research on multilayers is still in its 7 infancy. Here, we induce defects inside bulk MoS₂ through thermal 8 annealing and near the surface of multilayer MoS₂ using 375 nm 9 laser irradiation and investigate their photoluminescence (PL) and 10 fluorescence lifetime imaging. Enhanced emission is limited within 11 a certain MoS₂ thickness. The observed enhanced emission is 12 evidenced by a threshold behavior in superlinear PL intensity 13 increase, strong polarization effects, and increased lifetime of defect 14 peak. The laser power threshold for enhanced emission is much 15 smaller in defects near the surface than that inside the bulk of 16 multilayer MoS₂. The mechanical strain from a wrinkle in the 17 sample further lowers the laser power threshold for enhanced



18 emission. By exciting with a 639 nm laser that is close to the fundamental gap between the conduction band minimum and the 19 valence band maximum, the lifetime of defect enhanced emission increased by 5 times. Furthermore, one of the competing indirect 20 band gap emissions disappears, and the defect emission peak dominates the PL spectrum in the wrinkle area with a strain. The 21 discovered principle can be applied to future studies on the integration of enhanced emission and single photon emitters/single 22 photon emission involving selective depopulation of the conduction band of the host crystal to defect levels for quantum emitters.

23 KEYWORDS: photoluminescence, Raman, MoS₂, defect level, enhanced emission, fluorescence lifetime imaging, 2D materials

24 INTRODUCTION

25 The advent of two-dimensional (2D) materials has revolu-26 tionized the field of nanomaterials, offering unique properties 27 such as high integration density, tunable electronic and optical characteristics, and robust light-matter interactions. ¹⁻³ These 29 materials exhibit intriguing possibilities due to their point 30 defects, which can bestow them with a diverse array of 31 functionalities, including tunable electrical conductivity, 32 ferromagnetism,⁵ memristive behavior,^{6–8} and the ability to 33 serve as strain-controlled single photon emitter/single photon 34 emission (SPE). 9-11 In the quest to harness the full potential 35 of these defects, researchers have primarily focused on 2D 36 monolayers, where defect emission properties have been 37 thoroughly explored. 12-14 SPEs have been discovered in defect states of monolayer transition metal dichalcogenides (TMDs) 39 and h-BN monolayers mechanically exfoliated or grown by 40 chemical vapor deposition, such as MoS_{2} , 15,16 $MoSe_{2}$, 12,17 14 WSe_{2} , 13,18,19 WS_{2} , 20,21 $MoTe_{2}$, 22 and h-BN. 11,23,24 SPEs have 42 also been observed from multilayer samples of GaSe, 25,26 h-43 BN, 24 and oxidized WS₂ (i.e., WO₃). 27 SPE behavior and a 44 zero-phonon line clearly separated from phonon sidebands 45 were observed in multilayer h-BN.²⁴

The practical utility of these defects in monolayers is often 46 hindered by their susceptibility to oxidation under ambient 47 conditions, ²⁸ limiting their long-term stability and potential as 48 SPEs. The pursuit of technologically desirable defects has led 49 to the exploration of multilayer TMDs, which offer a unique 50 advantage: the ability to embed defects beneath the sample 51 surface, ensuring their long-term stability as SPEs. In a 52 thermal-annealed multilayer MoS₂, the defects embedded 53 inside the bulk can survive under high laser power, and the 54 defect induced photoluminescence (PL) peak (D-peak) shows 55 a superlinear intensity increase starting at 17 mW. ²⁹

Although our previously observed defect emission behavior 57 in bulk MoS₂ under thermal strain is striking²⁹—including 58 strong polarization effects and anomalously strong inten-59 sities—the puzzle remains as to why has this defect not been 60 reported so far, especially considering that TMD optical 61

 Received:
 June 18, 2024

 Revised:
 July 22, 2024

 Accepted:
 July 22, 2024



ACS Applied Optical Materials

106

129

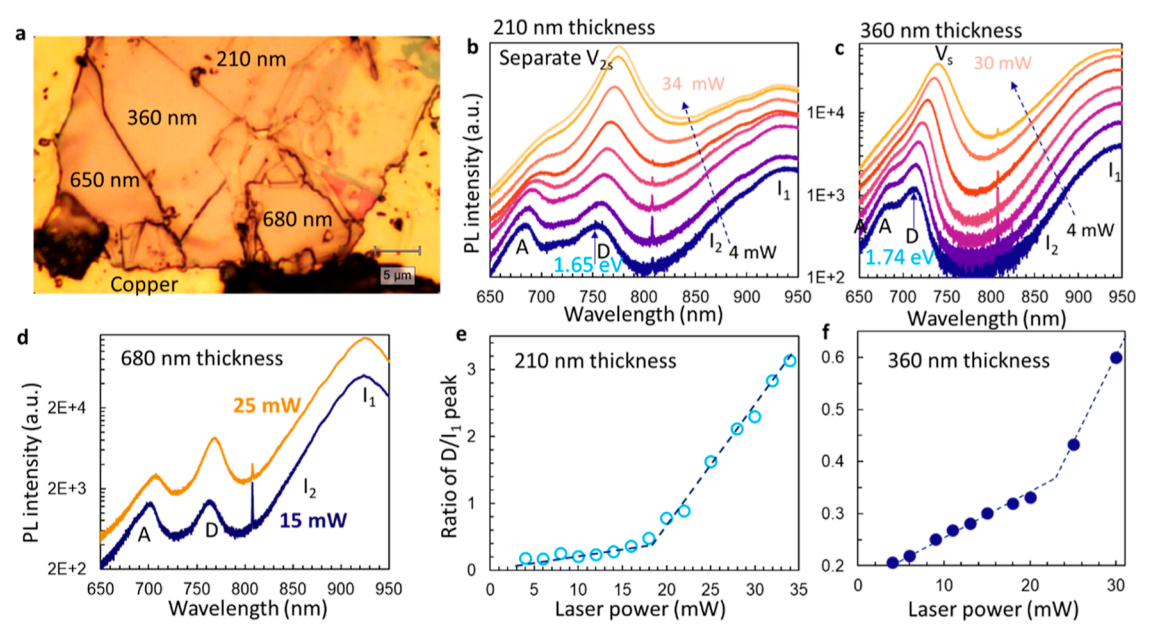


Figure 1. (a) Optical image of the multilayer MoS₂ sample with various thickness regions with embedded thermal defects. (b) PL spectra under laser powers of 4, 8, 12, 16, 20, 25, 32, and 34 mW for sample thickness of 210 nm. (c) PL spectra under laser powers of 4, 6, 9, 13, 18, 25, and 30 mW for sample thickness of 360 nm. (d) PL spectra under laser powers of 14 and 25 mW for a sample thickness of 680 nm. (e,f) Ratio of D peak to I peak, computed via peak fitting, as a function of laser powers for regions with thicknesses of 210 (e) and 360 nm (f).

62 properties have garnered the spotlight of 2D research for more 63 than a decade. There are the following two considerations. (1) 64 The focus of past work on few-layer and monolayer TMD 65 requires laser powers below ~1 mW to avoid thermal effects 66 and irreversibly damaging the TMD sheets. 30 Stronger laser 67 powers in the range of 5-20 mW lead to surface adsorption or 68 even thinning and etching. By contrast, bulk MoS_2 is 69 more resilient to laser irradiation, where laser-induced heat 70 may distribute throughout the bulk and dissipate more 71 efficiently.³⁰ This enables us to probe bulk MoS₂ defect 72 emission nondestructively under strong laser powers, contrary 73 to laser power restrictions usually prescribed for monolayers. 74 (2) Out of the two sets of sulfur vacancy levels—one 75 unoccupied set in the band gap and another occupied level 76 near the valence band edge—the latter is typically lower in energy than the valence band local maximum at the K point in monolayer and bulk MoS₂.³⁴ In monolayer MoS₂, this occupied level is not known to move above the valence band 80 maximum (VBM) at K under moderate strain (<5%). By 81 contrast, we previously showed that this occupied level moves 82 above the VBM at K under only 2% thermal strain (see, e.g., 83 Figure S11 of ref 29). This in turn sets up an effective two-level 84 system that allows direct interband emission between the 85 unoccupied and occupied sulfur vacancy levels without 86 participation of the bulk valence band edge at K (the other valence band valley at Γ has a much smaller optical matrix element with the midgap state). It is the unconventional combination of strong laser power applied nondestructively to bulk MoS₂ and the occupied vacancy level lifting off from the VBM under strain (unique to bulk MoS₂) that enables strong emission intensities and polarization effects in activated sulfur vacancies at room temperature.

In this study, to further verify previous theory predictions so and exact conditions for the enhanced emission, we design and produce S vacancies deep inside multilayer MoS₂ using two methods: thermal annealing introduces defects uniformly in bulk MoS₂, and UV 375 nm laser irradiation induces defects

near the surface of bulk MoS₂. By applying both thermal and 99 mechanical strain, enhanced emission occurs at a much lower 100 laser power for defects near the surface than those inside the 101 bulk. The defect (D) peak dominates in the PL spectrum, 102 while the indirect band gap emission disappears. The lifetime 103 of the D peak increases by 5 times when it is excited from 104 VBM to conduction band minimum.

EXPERIMENTAL METHODS

Preparation of Defects through Thermal Annealing

A free-standing thick MoS_2 was exfoliated by contacting Scotch tape 108 at the edge of bulk MoS_2 (2D semiconductor) and peeling it off. The 109 peeled sample was pressed onto copper-coated glass by polydime- 110 thylsiloxane (PDMS). It was annealed at 180 °C for 3 h on a hot plate 111 and then rapidly cooled to 0 °C in a fridge for 3 min. ²⁹ Then, the 112 sample was put in an ultrasonic vibration, where the uppermost loose 113 layers were removed. Thickness measurements were performed 114 through profilometer analysis.

Preparation of Defects through 375 nm Laser Irradiation 116

Multilayer MoS_2 with a thickness of 86 nm was obtained by the 117 exfoliation of bulk MoS_2 (2D semiconductor). The exfoliation process 118 involved the use of Scotch brand and thermal release tape as the final 119 step. We then placed the exfoliated multilayer MoS_2 onto a copper— 120 glass substrate and pressed it with PDMS. The substrate, with the 121 attached material, underwent heating at 100 °C until the thermal 122 release tape released the sample onto the substrate. The MoS_2 was 123 then irradiated with UV 375 nm laser (2 mm beam size, 8 mW) for 6 124 min. Thickness and wrinkle profiles were performed with the beam 125 profilometer. Because MoS_2 is not transparent to 375 nm, the UV 375 126 nm laser irradiation generates defects near the surface of multilayer 127 MoS_2 .

Raman and Photoluminescence Spectra

Most Raman and PL spectra measurements were carried out at room 130 temperature using a Renishaw inVia Raman Microscope. We 131 employed an 1800 lines/mm grating for these measurements, 132 covering a wavelength range of up to 950 nm. For the PL 133 measurement covering wavelengths up to 1050 nm, we employed a 134 1200 lines/mm grating. Throughout these measurements, a Cobolt 135

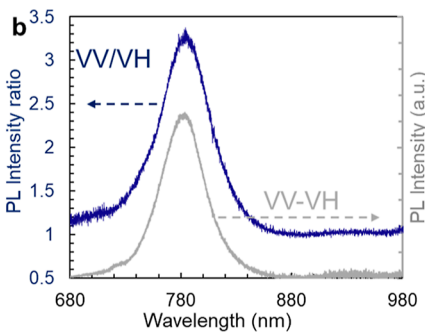


Figure 2. (a) PL spectra from 210 nm sample under 45 mW under VV (vertical vertical, dark blue) and VH (vertical horizontal, light blue) setups, where their intensities were normalized relative to I_1 . (b) The spectral ratio VV/VH and difference VV/VH for the 210 nm sample.

136 Samba 532 nm laser was utilized, coupled with a 50× objective lens 137 (numerical aperture NA = 0.5) with a working distance of 8.2 mm. 138 Precise laser power adjustments on the sample were achieved through combination of neutral density filters and laser power control 140 software provided by Cobolt Samba. The exposure time remained 141 consistently set at 10 s. Notably, 1 mW of laser power corresponded 142 to a laser intensity of 0.59 kW cm⁻², based on our optical setup; 143 hereafter we use laser power instead of laser intensity to document 144 our results. To explore Raman and PL polarization effects, a 145 broadband polarizing beam splitter cube (Thorlabs) was introduced 146 into the optical path of the Renishaw inVia, effectively handling 147 scattered light. This adjustment was necessitated by the fact that the 148 built-in polarizer in the Raman spectrometer had been optimized for 149 Raman polarization near 532 nm wavelength. We also studied the 150 Raman and PL measurements at room temperature using a 633 nm 151 laser coupled with a 50× objective lens (numerical aperture NA = 152 0.5). A heating/cooling stage (Linkam THMS600) was mounted on 153 the microscope for in situ low-temperature Raman and PL analysis.

154 Fluorescence Lifetime Imaging

155 The fluorescence lifetime imaging (FLIM) and its lifetime histogram 156 for A-peak and D-peak in the sample of defects near the surface of 157 multilayer MoS₂ were measured in a Micro Time 200 time-resolved 158 confocal fluorescence microscope. Photon detection events were 159 meticulously recorded by using a PicoQuant PicoHarp 300 time-160 correlated single-photon-counting system. Two Picosecond (PS) 161 lasers were used for the excitation of PL. One picosecond laser has a 162 wavelength of 639 nm, a repetition rate of 80 MHz, and an average 163 power of 1.63 mW. The other has a wavelength of 405 nm, a 164 repetition rate of 80 MHz, and an average power of 3.84 mW. The 165 confocal microscope was equipped with a 20× objective lens 166 (numerical aperture NA = 0.4). The confocal microscope used a 167 20× objective lens (numerical aperture NA = 0.4) with a working 168 distance of 12.0 mm. To reduce the height variation effect around the 169 wrinkle, the piezo stage was set to scan the crest of the wrinkle. 170 Scanning a large area results in the variation of the lifetime event 171 number. Data acquisition and subsequent analysis were seamlessly 172 executed by using SymPho-Time 64 software.

173 Results of PL Measurement and Enhanced Emission in 174 Thermally Annealed MoS₂

175 In this section, we focus on the first type of defective sample obtained 176 by thermal annealing and explore the relationship between the 177 thickness of our multilayer MoS_2 sample and the enhanced emission 178 arising from defects. Figure 1a shows an optical image of the 179 multilayer MoS_2 sample, showcasing various thickness regions 180 obtained through a profilometer analysis. Laser power-dependent 181 PL spectra across three different regions of the sample, as depicted in 182 Figure 1b–d, corresponding to thicknesses of 210, 360, and 680 nm, 183 respectively. In Figure 1b,d, the D peak is around 751 nm (1.65 eV) 184 excited by a low laser power, associated with a defect that has been 185 tentatively attributed to V_{25} (disulfur vacancy) following the 186 calculated band gaps of the oxygen passivated S-defects in Table S2 187 in the Supporting Information of ref 28 The D peak in Figure 1c is

around 713 nm (1.74 eV), which we attribute to V_S (sulfur vacancy) 188 following the atomic force microscopy images, ³⁴ comparison of PL 189 measurement and density functional theory (DFT) calculations ^{29,34} 190 (also in Table S2 of the ref 28). All samples and defects survive under 191 high laser powers up to 34 mW. The PL intensities of the A-peak (free 192 exciton peak) and I_1 peak (indirect band gap emission) increase 193 linearly with the laser power. ²⁹ There is no enhanced emission from 194 the sample with a thickness of 680 nm in Figure 1d as the ratio of the 195 D peak intensity over the I_1 -peak intensity is the same under 15 and 196 25 mW

Figure 1e,f illustrates the intensity ratio of the D-peak over the I₁- 198 peak, computed via peak fitting, for regions with thicknesses of 210 199 and 360 nm. The intensity ratio shows two linear increases fitted with 200 two different slopes, as indicated by the dashed line in Figure 1e for 201 210 nm thickness. The D-peak is considered to exhibit enhanced 202 emission, initiating at a laser power threshold of 19 mW. This 203 transition was previously attributed to the K_C valley replacing the Q_C 204 valley as the CBM as it becomes populated by carriers, relaxing them 205 from $K_{\rm C}$ valley to defect levels, and consequently leading to enhanced 206 emission in three-level energy system. ²⁹ A similar intensity ratio with 207 two distinguished regions occurs in Figure 1f for the sample with a 208 thickness of 360 nm. The enhanced emission of the D peak is 209 triggered at a laser power of 24 mW. These results underscore the 210 profound influence of sample thickness on the thermal strain-enabled 211 enhanced emission. Specifically, thinner multilayer samples (210 nm) 212 exhibit enhanced emission at relatively lower laser powers (19 mW), 213 while the 360 nm sample, although exhibiting enhanced emission, did 214 so at higher laser powers (24 mW). Notably, the 680 nm thick region 215 failed to manifest enhanced emission even under the influence of a 216 higher laser power (25 mW).

We checked the Raman spectrum under laser powers of 4 and 25 218 mW as shown in Figure S1a for the sample thickness of 210 nm and in 219 Figure S1b for 360 nm. The Raman E_{2g} and A_{1g} peak wavenumbers 220 change by 3.02 and 2.67 cm⁻¹ for the sample with a thickness of 210 221 nm, respectively, when the laser power is changed from 4 to 25 mW. 222 For the sample with a thickness of 360 nm, E_{2g} and A_{1g} peak 223 wavenumbers change by 3.22 and 2.87 cm⁻¹ for the laser power from 224 4 to 25 mW. Usually, the Raman peak red-shifts with increasing 225 temperature from lattice thermal expansion.²⁹ It means the thicker 226 sample (360 nm) may have a higher temperature than the 210 nm 227 sample due to more absorption in a thicker sample. The defect type is 228 the same in Figure 1b,d, so we compare the Raman peak under a laser 229 power of 25 mW. The Raman E_{2g} and A_{1g} peaks are located at 380.69 $\,$ 230 and 406.55 cm⁻¹, respectively, for 210 nm thickness, while they are at 231 380.35 and 405.97 cm⁻¹ for 680 nm thickness. Again, this may be 232 attributed to the thicker sample (680 nm) having a higher 233 temperature. Considering both the temperature and thickness effects, 234 the sample thickness plays a crucial role in the observation of 235 enhanced emission.

We also measured the polarization effect for the 210 nm sample 237 under a laser power of 45 mW. Figure 2a shows normalized PL 238 f2 spectra relative to the $\rm I_1$ peak for polarizations of VV (vertical 239 excitation, vertical scattered signal) and VH (vertical excitation, 240

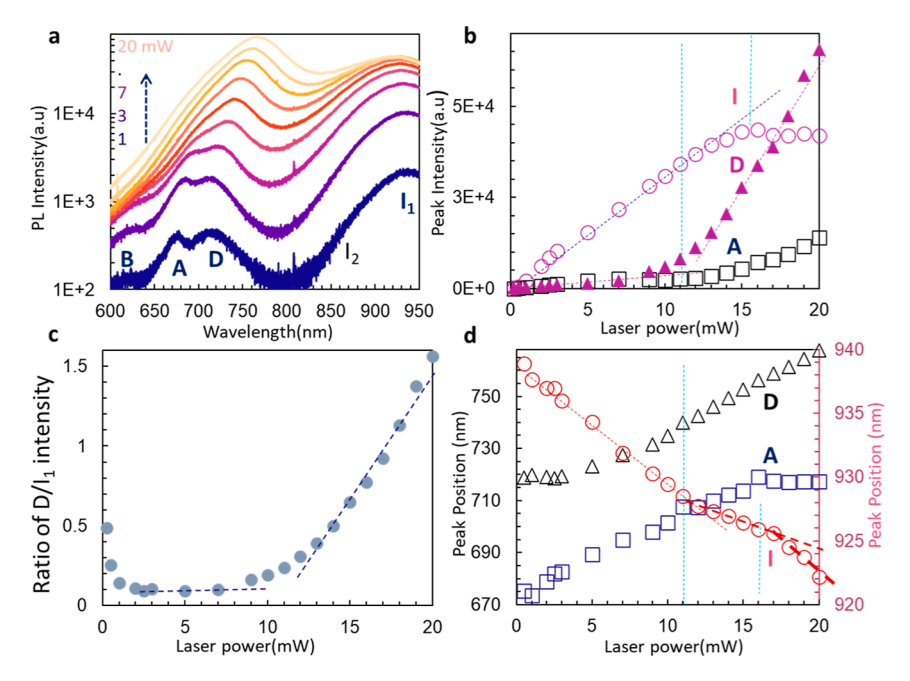


Figure 3. (a) PL spectra of UV laser irradiation-induced defects in flat multilayer MoS_2 under laser powers of 1, 3, 7, 10, 12, 14, 16, 18, and 20 mW from the bottom to the top. (b) PL peak intensity for A-peak (squares), D-peak (triangles), and I-peak (circles) as a function of laser power. (c) The ratio of D peak to I_1 peak intensity, computed via peak fitting, as a function of laser powers. (d) PL peak positions as a function of laser power where primary axis represents the peak positions for D-peak and A-peak, and secondary axis represents the peak position for I_1 -peak.

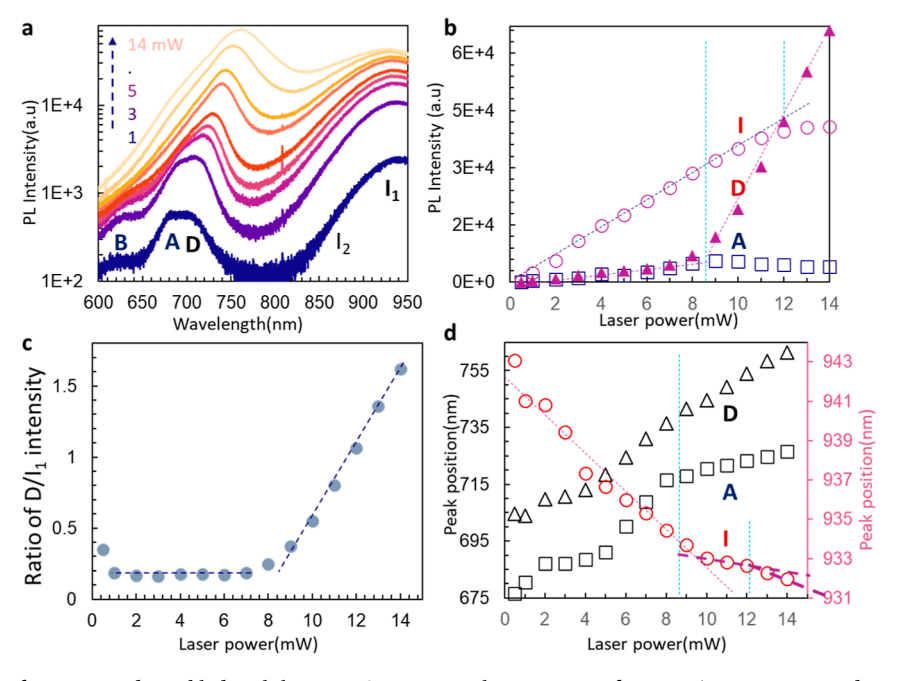


Figure 4. (a) PL spectra of UV exposed wrinkled multilayer MoS_2 at various laser powers of 1, 3, 5, 6, 7, 9, 10, 12, and 14 mW from bottom to top using 523 nm laser. (b) PL peak intensity for A-peak (squares), D-peak (triangles), and I-peak (circles) as a function of laser power. (c) The ratio of D peak to I_1 peak intensity, computed via peak fitting, as a function of laser powers. (d) Peak positions as a function of laser power where primary axis represents the peak positions for D-peak and A-peak, and secondary axis represents the peak position for I-peak.

 $_{241}$ horizontal scattered signal). The A, D, and I_1 peaks are clearly $_{242}$ separated in Figure 2a. The ratio of the VV spectrum over VH and the $_{243}$ difference in VV and VH spectra are shown in Figure 2b. Polarization $_{244}$ effects can be seen wherever the ratio deviates significantly from unity. $_{245}$ Clearly, VV/VH and VV/VH curves have peaks centered at D-peak. There is no feature at wavelengths for the A and I_1 peaks. As seen $_{247}$ from Figure 2, the D-peak in the PL spectra is highly polarized, $_{248}$ presumably due to it originating from enhanced emission.

Results from MoS₂ with Defects Induced by UV Laser

Next, we focus on the second type of defective sample obtained by 251 UV laser irradiation. The thickness of the multilayer MoS₂ sample is 252 determined to be 86 nm using profilometer as shown in Figure S2a for 253 the optical image and in Figure S2b for the height profile. A wrinkle in 254 the sample can be seen in the bottom right corner of Figure S2a and is 255 characterized separately in Figure S3. Figure S3a,b shows the optical 256 image and height profile for this wrinkle in the sample, respectively. 257

249 250

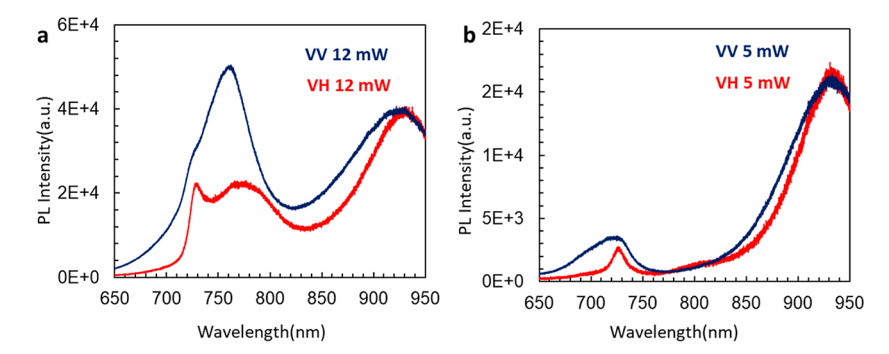


Figure 5. Polarization-dependent PL spectra on UV exposed wrinkle region on multilayer MoS₂ with 532 nm laser, at 12 (a) and 5 mW (b) under VV (blue) and VH (red) setups, where their intensities normalized relative to the I-peak.

258 The wrinkle has a height of 3.53 μm and a width of 27.1 μm as shown 259 in Figure S3b, where PL and FLIM were recorded. After the sample is 260 irradiated by a UV 375 nm laser for 6 min, S vacancies have been 261 generated. For the long-term stability of defects and for data 262 management purposes, we coated the sample with 30 nm Al_2O_3 by 263 atomic layer deposition at 150 °C.

The D peak at the flat sample region has a wavelength of 718.8 nm 265 and 0.5 mW. Figure 3a shows the PL spectra at a flat multilayer MoS₂ 266 region under different laser powers of 1, 3, 7, 10, 12, 14, 16, 18, and 267 20 mW. The A and B peaks (both from free excitons), D peak, and I 268 peak are observed. Notably, for lower laser powers, the I-peak 269 exhibited higher intensities compared with the D-peak. As the laser 270 power increased, the D-peak intensity surpassed that of the I peak. We 271 presented peak-fitted data in Figure 3b,c, illustrating laser power-272 dependent PL intensities and their ratio, and in Figure 3d, illustrating 273 power-dependent PL peak positions. From Figure 3b, both the A-peak 274 (squares) and the I-peak (circles) exhibited linear growth from 1 to 275 15 mW, whereas the D-peak (triangles) demonstrated a superlinear 276 increase. Enhanced emission occurs above a laser power of 277 approximately 11 mW, again attributed to efficient relaxation of 278 carriers from $K_{\rm C}$ valley to defect levels which cause population 279 inversion in the defect level. ²⁹ Due to the crossover of $K_{\rm C}$ and $Q_{\rm C}$ valley (Q_C valley is higher in energy than the K_C valley after the transition), the steady-state carrier population becomes depleted in Q_C valley, which decreases I₁ intensity. That is exactly what we have 283 observed for I intensity above 15 mW (indicated by the second dashed blue line in the vertical direction). The ratio of D/I_1 intensities 285 in Figure 3c also shows a laser power threshold of 11 mW for the 286 enhanced PL emission.

We next fitted the PL spectrum to extract the wavelengths of all 288 peaks. As seen from Figure 3d, the wavelengths of the A peak 289 (squares) and the D peak (triangles) increase with the increasing laser 290 power due to laser-induced thermal strain, as predicted previously by 291 DFT calculations. ²⁹ At the threshold laser power of 11 mW, the D 292 peak wavelength is 740 nm, almost the same as the calculated 293 threshold wavelength of 738 nm. The decreasing of I-peak wavelength 294 slows down after 11 mW in Figure 3d after the crossover of $K_{\rm C}$ and $Q_{\rm c}$ 295 valley, as indicated by dashed red lines for slopes.

We also studied the shift in Raman peaks of E_{2g} and A_{1g} as we 297 increased the laser power in Figure S4. Increasing the laser power 298 from 0.5 to 11 mW (starting point for the enhanced emission), E_{2g} and A_{1g} peak wavenumbers changed by 3.52 and 3.27 cm⁻¹, indicating 300 an effective temperature increase locally under laser irradiation by 265 301 K. ²⁹ The increased thermal strain enables the crossover of the $K_{\rm C}$ and 302 $Q_{\rm C}$ valley, leading to enhanced emission. ²⁹

To understand the effect of mechanical strain, we then studied the 304 PL on a wrinkle in our multilayer MoS₂ sample. It is a naturally 305 formed wrinkle that occurred during the squeezing of air between 306 MoS₂ and the substrate. The D peak on the wrinkle has a wavelength 307 of 704.7 nm (1.76 eV) at 0.5 mW, same wavelength as the one 308 produced by a UV lamp. Eigure 4a shows the PL spectra on the 309 wrinkle at various laser powers of 1, 3, 5, 6, 7, 9, 10, 12, and 14 mW. 310 Similar to the flat region discussed above, the two free exciton peaks A

and B, defect peak D, and indirect band gap peak I are observed. Also 311 similar is the D peak surpassing the I peak in intensity at high laser 312 powers, as observed in the flat region. To get a clearer picture of this 313 phenomenon, we present the peak fitted data in Figures 4b,c 314 indicating the laser power-dependent PL peak intensity and their 315 ratio, and in Figure 4d, the laser power-dependent PL peak position. 316 From Figure 4b, we noticed a linear increase in PL peak intensity for 317 the A peak (square) and I peak (circle) from 1 to 10 mW, whereas the 318 D peak (triangles) showed a superlinear behavior with increasing laser 319 power. From the D peak intensity change, the enhanced emission can 320 be estimated to start at 8.5 mW. The laser power threshold of 8.5 mW 321 for the enhanced PL emission is also confirmed in the ratio of D/I₁ 322 intensities in Figure 4c. Due to the mechanical strain from the wrinkle 323 in addition to the generated thermal strain, the laser power required 324 to enable enhanced emission in the wrinkle is lower than that in the 325 flat region. It corresponds to a lower laser power of 8.5 mW for the 326 enhanced emission in Figure 4b than 11 mW in Figure 3b. In 327 multilayer MoSe₂, the threshold laser power is near 2 mW when the 328 MoSe₂ is under both thermal and mechanical strain.³⁶ Above 12 mW 329 laser power in Figure 4b, the I peak intensity increases sublinearly, 330 indicated by the second vertical blue line. It is again due to the strain- 331 enabled shifting of the Q_C valley above the K_C valley.

The fitting of the PL spectrum gives a D peak wavelength of 738.9 333 nm on average and an A peak wavelength of 718.0 nm at 8.5 mW laser 334 power in Figure 4d, almost the same as the previously calculated 335 values of 738 and 717 nm, respectively, at 1% strain. The decreasing 336 of I peak wavelength slows down after the threshold laser power of 8.6 337 mW after the crossover of the $K_{\rm C}$ and $Q_{\rm C}$ valley, as indicated by 338 dashed red lines for slopes in Figure 4d. We also studied the shift in 339 Raman peaks of $E_{\rm 2g}$ and $A_{\rm 1g}$ as we increased the laser power in Figure 340 S5. Increasing the laser power from 0.5 to 9 mW, $E_{\rm 2g}$ and $A_{\rm 1g}$ peak 341 wavenumbers change by 4.52 and 3.98 cm⁻¹, indicating an increase in 342 the effective local temperature by 331 K.²⁹

To confirm that the enhanced emission started at the laser power of 344 8.5 mW on the wrinkle, we conducted polarization studies. 29,37 We 345 examined the polarization-dependent PL spectra at two laser powers: 346 one below the threshold (5 mW) and one above the threshold (12 347 mW). Figure 5a,b illustrates the polarization-dependent PL spectra 348 f5 acquired at 12 and 5 mW, respectively, on the wrinkle. We aligned the 349 I peak of the spectra from both vertical-vertical (VV, blue) and 350 vertical-horizontal (VH, red) polarization setups. From Figure 5a, it 351 is evident that the intensity of the D peak (760 nm) for VH (red) is 352 notably lower than the intensity of the D peak (760 nm) for VV 353 (blue) at 12 mW. Conversely, Figure 4b shows that the VV (blue) 354 and VH (red) curves exhibit similar D peak (730 nm) intensities at 5 355 mW. We did peak fitting for both graphs and checked the intensity 356 ratio of the D peak (VV/VH) for both 12 and 5 mW. The intensity 357 ratio for the D peak is found to be 1.03 for 5 mW and 2.38 for 12 358 mW. This shows that there is a polarization effect for the D peak at 12 359 mW but not at 5 mW due to 8.5 mW threshold of enhanced emission 360 on the wrinkle. We also studied the polarization-dependent Raman 361 spectra to prove that the VV and VH setups provided us with the 362 parallel and perpendicular polarization PL spectra, respectively, in 363

ACS Applied Optical Materials

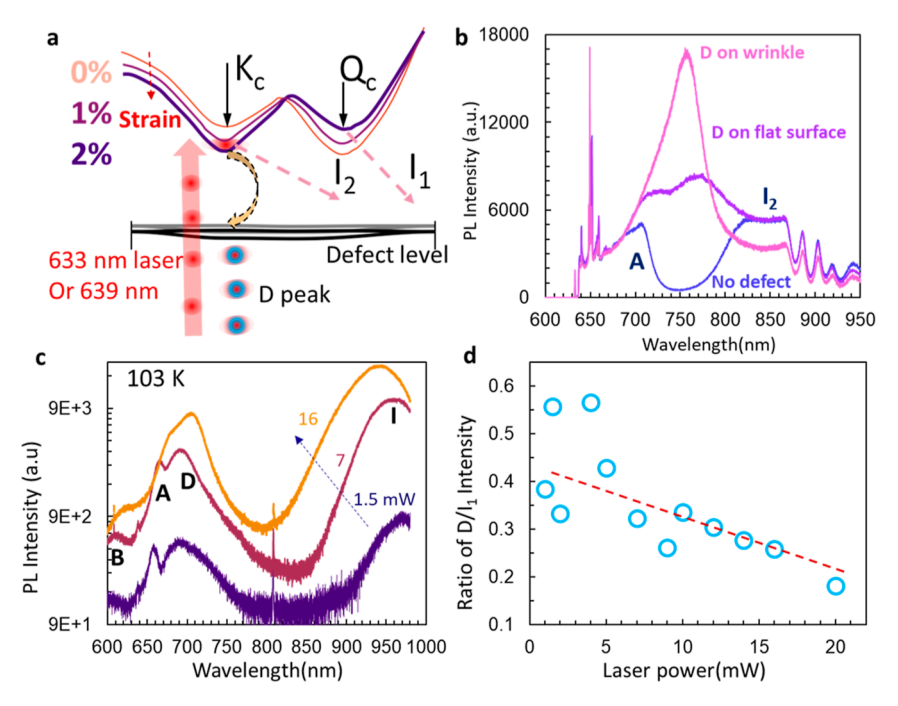


Figure 6. (a) Schematic of the band structure of bulk MoS_2 under different thermal strains. The 633 or 639 nm laser can pump electrons to K_c only. (b) PL spectra from a multilayer MoS_2 without defects (dark blue line), with defects in flat region (dark purple line), and with defects in a wrinkle with a mechanic strain (pink line), excited by 633 nm. (c) PL spectra of UV laser irradiation-induced defects in flat multilayer MoS_2 at 103 K, excited by 532 nm laser. (d) The ratio of the D peak to I_1 peak intensity, computed via peak fitting, as a function of laser powers.

364 Figure S6. Raman spectra in the VH setup do not contain the $A_{\rm lg}$ 365 modes.

66 DISCUSSIONS

367 In the thermally annealed multilayer MoS2, we also observed 368 the enhanced emission for a defect level near 784 nm, as 369 shown in Figure S7. However, there is no enhanced emission 370 from the defect levels when both PLs from the Vs defect (labeled as D₁ in Figure S8) and one near 810 nm (labeled as 372 D₂) appear in multilayer MoS₂ near the edge of the 210 nm 373 sample in Figure 1a due to the splitting of electrons from K_c to 374 two defect levels. The intensity ratio of D₁/I₁ decreases, while 375 D₂/I₁ increases linearly with the increasing laser power in 376 Figure S8. The defects in thermally annealed multilayer MoS₂ are stable, and the observed enhanced emission is reproducible after the sample was kept in lab atmospheric conditions for 10 months and remeasured. In a thin sample MoS2 with a thickness of 25 nm, peaks near 583 nm that are related to a burned sample³⁸ have been observed when the laser power 382 reached 8 mW, as shown in Figure S9. Based on our 383 observation, the optimal thickness range for achieving enhanced emission is between 25 and 360 nm. The safe 385 operational window for laser powers is up to 30 mW for the 386 thermally annealed multilayer MoS₂.

The safe operation window for laser powers is up to 22 mW sas for the UV laser irradiated multilayer MoS₂, as shown in Figure S10, where the optical image shows a burned sample under a most laser power of 24 mW. In another UV-irradiated multilayer MoS₂ with a thickness of 89 nm, the laser power of up to 25 mW can be used for the enhanced emission, as shown in Figure S11. These UV-induced effects were stable for 14 months. The lower operation window for laser powers in UV sps laser-induced defects than in thermally annealing-induced ones is due to the existence of defects closer to the sample surface. After 14 months, the sample in Figures 3 and 4 was cooled

down to 103 K and warmed up to room temperature. The 398 enhanced emission from defects of such a sample is 399 reproducible, as shown in Figure S10. In UV-irradiated 400 multilayer MoS₂ with a thickness of 10 nm, the sample was 401 burned under a laser power of 5 mW (Figure S12). The 402 optimal thickness range for achieving enhanced emission from 403 UV-induced defect is expected between 35 (i.e., 25 + 10) and 404 350 (i.e., 360–10) nm.

A more detailed computational analysis leads to further 406 experimental studies below. Figure 6a shows a schematic of the 407 f6 multilayer MoS₂ band structure based on our previous work 408 (see Figure S11 of ref 29). The band structures for increasing 409 strain are plotted with darker colors. The strain engineering has 410 resulted in a crossover of K_c and Q_c (i.e., the energy level of K_c 411 is lower than Qc for bulk MoS2 under thermal strains). As 412 shown in the diagram, a carefully selected excitation laser 413 (using 633 nm in PL and 639 nm in FLIM) pumps the 414 electron to the K_c valley only. Above the threshold strain, the 415 pristine Q_{C} - Γ_{V} (I_{1}) indirect band gap crosses over to the K_{C} - Γ_{V} 416 (I2) indirect band gap, resulting in more effective carrier 417 relaxation from the $K_{\rm C}$ valley to the defect level.²⁹ We next 418 consider another possibility of pumping carriers only to the $K_{\rm C}$ 419 valley, which eliminates I₁ from the PL spectrum and 420 potentially allows carriers to relax more efficiently to the 421 defect level. So, we studied the PL spectra by exciting MoS₂ 422 with a 633 nm laser that is close to the fundamental gap 423 between the conduction band minimum and the VBM in our 424 multilayer MoS₂ under different conditions. Figure 6b shows 425 the PL spectra from our multilayer MoS₂ without defects (dark 426 blue line), with defects in the flat region (dark purple line), and 427 with defects in a wrinkle with a mechanic strain (pink line), 428 excited by a 633 nm laser. There is no I1 emission in all PLs 429 because there is no carrier in the Q_c valley. In the sample with 430 defects, the A peak has an intensity similar to that of I2 431 emission. The D-peak has a higher intensity than the I_2 432

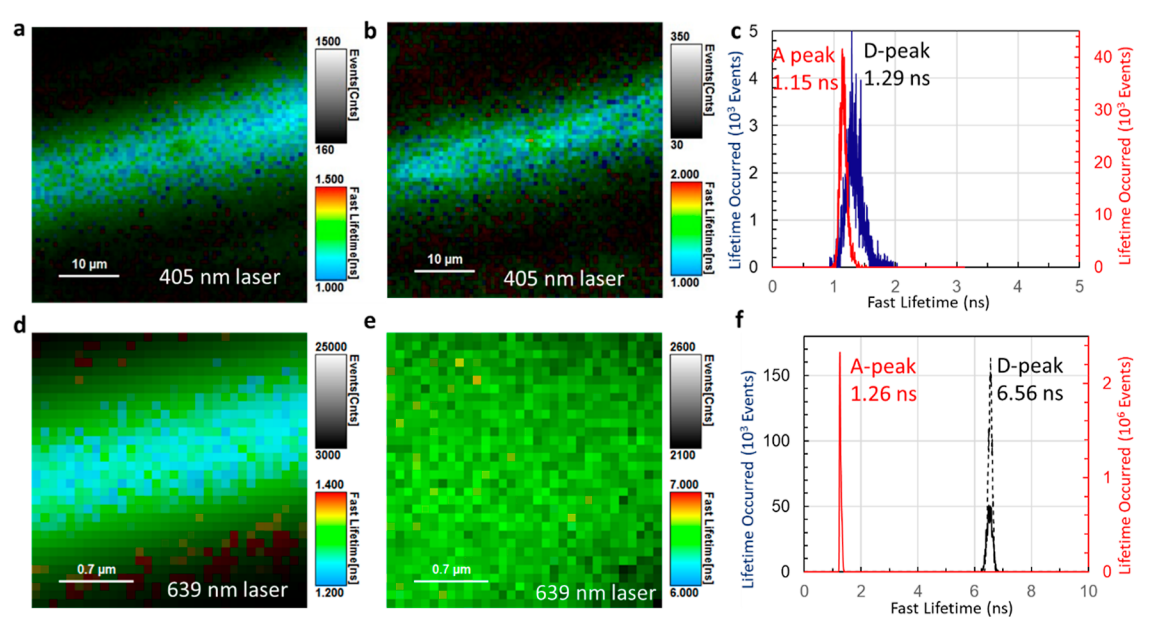


Figure 7. (a) FLIM measurement of the wrinkle region using a 700 ± 20 nm bandpass filter when the PL is excited by a 405 nm laser. (b) FLIM measurement of the wrinkle region using a 750 ± 20 nm bandpass filter when the PL is excited by a 405 nm laser. (c) Lifetime histogram obtained from FLIM when the PL is excited by a 405 nm laser. (d) FLIM measurement of the whole wrinkle region using a 700 ± 20 nm bandpass filter when the PL is excited by a 639 nm laser. (e) FLIM measurement of the whole wrinkle region using a 750 ± 20 nm bandpass filter when the PL is excited by a 639 nm laser. (f) Lifetime histogram obtained from FLIM when the PL is excited by a 639 nm laser.

 433 emission in the flat sample. With a strain in the wrinkle, the D 434 peak dominates in the PL, and $\rm I_2$ emission has less intensity 435 than those in samples without the mechanic strain.

To further test the thermal-strain effect, we cooled the multilayer MoS_2 in Figure 3 to 103 K. Figure 6c shows the PL spectra of UV laser irradiation-induced defects under laser powers of 1.5, 7, and 16 mW of the 532 nm laser. Figure 6d shows the decreasing ratio of the D peak to I_1 peak intensity with increasing laser powers. There is no enhanced emission when the sample is at 103 K. The same sample shows the enhanced emission at room temperature in Figure S10, measured after Figure 6c,d. These results indicate that thermal strain in MoS_2 at the low temperature is not high enough for the crossover of K_c and Q_c .

To determine the lifetime of the carrier, we studied the 448 FLIM of the wrinkle region. Figure S13 shows an optical image 449 of the wrinkle. Figure 7a,b shows the FLIM measurement of 450 the A and D peaks, respectively, in the wrinkle when the PL is 451 excited by a 405 nm laser. The corresponding lifetime 452 histogram is shown in Figure 7c, where the lifetimes for A 453 and D peak are 1.15 and 1.29 ns, respectively. Under 639 nm 454 laser excitation, the FLIM measurement of the wrinkle region 455 for A and D peaks and the corresponding lifetime histogram 456 are shown in Figure 7d-f, respectively. The lifetime is 457 measured to be 6.56 ns for the D peak and 1.26 ns for the 458 A peak, as shown in Figure 7f. The dashed and solid blue lines 459 are data from two different measurements for checking the 460 reproducibility. Achieving population inversion necessitates a 461 difference in lifetime between competing excited states, and the 462 presence of these two distinct peaks in the lifetime histogram 463 strongly indicates such a difference. The FLIM unequivocally 464 reveals the existence of an enhanced emission from the D peak, 465 consistent with our earlier findings.

In the future, a carefully selected laser can pump electrons to 467 K_c only then the electrons jump from K_C to the point defects 468 by integrating a resonant cavity with the sample, resulting in

SPE with high brightness.³⁹ To achieve the SPE, defects are 469 created in vacuum, primarily associated with unpassivated Vs 470 (only Vs defects are observed in UV-irradiated multilayer 471 MoS₂ in this study). The defect density should be controlled 472 by adjusting the laser power or exposure time. The beam 473 control and manipulation of UV laser are easier than the ion 474 beam. Recently, we applied UV laser to the sample through an 475 objective lens. Finding the relationship between the defect 476 peak strength and the Gaussian distribution of the UV laser 477 power is very efficient. In multilayer MoS₂, raising the 478 temperature instead of cooling the sample might be necessary 479 to observe the SPE. Deterministic strain patterning in 480 multilayer MoS₂ will be a challenge. Another challenge is to 481 characterize the defects at the atomic level. Scanning tunneling 482 microscopy (STM)³⁴ and dark-field scanning transmission 483 electron microscopy (ADF-STEM)⁴⁰ imaging are effective in 484 characterizing defects in monolayer MoS2. It is challenging to 485 locate the defects in bulk MoS₂ by STM and ADF-STEM.

SUMMARY

In this study, we generated and studied S vacancies in 488 multilayer MoS₂ through thermal annealing and through UV 489 375 nm laser irradiation. Our study of the defects in the bulk 490 underscores the profound influence of sample thickness on the 491 thermal strain-enabled enhanced emission. Even though the 492 thick samples absorb more temperatures, enhanced emission 493 occurs only within a limited thickness of the sample. The laser 494 threshold for enhanced emission from surface defects is 495 observed to have a lower value compared to the bulk defects. 496 The threshold can be further reduced if we could combine 497 mechanical strain with the thermal strain. When an excitation 498 near the fundamental band gap is applied to the defect on 499 wrinkles, we can make the defect emission prominent in the PL 500 spectra by eliminating the indirect I₁ emission. Such an 501 excitation would also increase the lifetime of enhanced 502 emission by 5 times that of the A peak emission.

487

559

567

504 ASSOCIATED CONTENT

505 Supporting Information

The Supporting Information is available free of charge at 507 https://pubs.acs.org/doi/10.1021/acsaom.4c00276.

Laser power and sample thickness-dependent Raman spectra from flat and strained multilayer MoS₂, optical images from beam profilometer, polarization-dependent Raman spectra, PL spectra under laser powers, PL spectra from a sample with two defect lines under different laser powers, PL spectra of thin samples with thicknesses of 25 and 10 nm, and PL spectra for checking the defect stability and reproducibility of enhanced emission (PDF)

517 **AUTHOR INFORMATION**

518 Corresponding Author

Yuankun Lin — Department of Physics, University of North
Texas, Denton, Texas 76203, United States; Department of
Electrical Engineering, University of North Texas, Denton,
Texas 76203, United States; ○ orcid.org/0000-0001-5691589X; Email: yuankun.lin@unt.edu

Sinto Varghese - Department of Physics, University of North

524 Authors

525

538

539

540

541

542

543

544

545

546

547

548

549

550

551

552

508

509

510

511

512

513

514

515

516

Texas, Denton, Texas 76203, United States 526 Noah Hurley - Department of Physics, University of North 527 Texas, Denton, Texas 76203, United States 528 Steve Kamau - Department of Physics, University of North 529 530 Texas, Denton, Texas 76203, United States Yan Jiang – Department of Physics, University of North Texas, 531 Denton, Texas 76203, United States 532 Roberto Gonzalez Rodriguez - Department of Physics, 533 University of North Texas, Denton, Texas 76203, United 534 States; orcid.org/0000-0001-6849-1799 535 Bhojraj Bhandari - Department of Physics, University of 536 North Texas, Denton, Texas 76203, United States 537

Tengteng Lyu — Department of Chemistry, University of North Texas, Denton, Texas 76203, United States

Hao Yan — Department of Chemistry, University of North Texas, Denton, Texas 76203, United States; orcid.org/

0000-0003-4894-5620

Yuanxi Wang — Department of Physics, University of North
Texas, Denton, Texas 76203, United States

Anupama B. Kaul — Department of Electrical Engineering and Department of Materials Science and Engineering, University of North Texas, Denton, Texas 76203, United States;
orcid.org/0000-0003-4052-8064

Jingbiao Cui — Department of Physics, University of North Texas, Denton, Texas 76203, United States; Department of Chemistry, Department of Electrical Engineering, and Department of Materials Science and Engineering, University of North Texas, Denton, Texas 76203, United States;

orcid.org/0000-0003-3408-1016

sss Complete contact information is available at: ss6 https://pubs.acs.org/10.1021/acsaom.4c00276

557 Notes

558 The authors declare no competing financial interest.

ACKNOWLEDGMENTS

J.C. and Y.L. acknowledge partial financial support from U.S. 560 National Science Foundation, grant number 2128367. A.K. and 561 Y.L. acknowledge partial financial support by the Department 562 of Energy/National Nuclear Security Administration under 563 Award Number DE-NA0004114. Y.W. acknowledges startup 564 funds from UNT and partial support from NSF DMR- 565 2340733.

REFERENCES

- (1) Iff, O.; Buchinger, Q.; Moczała-Dusanowska, M.; Kamp, M.; 568 Betzold, S.; Davanco, M.; Srinivasan, K.; Tongay, S.; Antón-Solanas, 569 C.; Höfling, S.; Schneider, C. Purcell-Enhanced Single Photon Source 570 Based on a Deterministically Placed WSe 2 Monolayer Quantum Dot 571 in a Circular Bragg Grating Cavity. *Nano Lett.* **2021**, 21 (11), 4715–572 4720.
- (2) Klein, J.; Sigl, L.; Gyger, S.; Barthelmi, K.; Florian, M.; Rey, S.; 574 Taniguchi, T.; Watanabe, K.; Jahnke, F.; Kastl, C.; Zwiller, V.; Jöns, K. 575 D.; Müller, K.; Wurstbauer, U.; Finley, J. J.; Holleitner, A. W. 576 Engineering the Luminescence and Generation of Individual Defect 577 Emitters in Atomically Thin MoS₂. ACS Photonics **2021**, 8 (2), 669–578 677.
- (3) Iff, O.; Tedeschi, D.; Martín-Sánchez, J.; Moczała-Dusanowska, 580 M.; Tongay, S.; Yumigeta, K.; Taboada-Gutiérrez, J.; Savaresi, M.; 581 Rastelli, A.; Alonso-González, P.; Höfling, S.; Trotta, R.; Schneider, C. 582 Strain-Tunable Single Photon Sources in WSe₂Monolayers. *Nano Lett.* 583 **2019**, *19* (10), 6931–6936.
- (4) Gao, H.; Suh, J.; Cao, M. C.; Joe, A. Y.; Mujid, F.; Lee, K. H.; S85 Xie, S.; Poddar, P.; Lee, J. U.; Kang, K.; Kim, P.; Muller, D. A.; Park, J. S86 Tuning Electrical Conductance of MoS₂Monolayers through Substituses tional Doping. *Nano Lett.* **2020**, 20 (6), 4095–4101.
- (5) Zhang, F.; Zheng, B.; Sebastian, A.; Olson, D. H.; Liu, M.; S89 Fujisawa, K.; Pham, Y. T. H.; Jimenez, V. O.; Kalappattil, V.; Miao, L.; S90 Zhang, T.; Pendurthi, R.; Lei, Y.; Elías, A. L.; Wang, Y.; Alem, N.; S91 Hopkins, P. E.; Das, S.; Crespi, V. H.; Phan, M.; Terrones, M. S92 Monolayer Vanadium-Doped Tungsten Disulfide: A Room-Temper- S93 ature Dilute Magnetic Semiconductor. *Advanced Science* **2020**, *7* (24), S94 2001174.
- (6) Sangwan, V. K.; Lee, H. S.; Bergeron, H.; Balla, I.; Beck, M. E.; 596 Chen, K. S.; Hersam, M. C. Multi-Terminal Memtransistors from 597 Polycrystalline Monolayer Molybdenum Disulfide. *Nature* **2018**, 554 598 (7693), 500–504.
- (7) Ge, R.; Wu, X.; Kim, M.; Shi, J.; Sonde, S.; Tao, L.; Zhang, Y.; 600 Lee, J. C.; Akinwande, D. Atomristor: Nonvolatile Resistance 601 Switching in Atomic Sheets of Transition Metal Dichalcogenides. 602 Nano Lett. 2018, 18 (1), 434–441.
- (8) Xu, R.; Jang, H.; Lee, M. H.; Amanov, D.; Cho, Y.; Kim, H.; 604 Park, S.; Shin, H. J.; Ham, D. Vertical MoS₂ Double-Layer Memristor 605 with Electrochemical Metallization as an Atomic-Scale Synapse with 606 Switching Thresholds Approaching 100 MV. *Nano Lett.* **2019**, *19* (4), 607 2411–2417.
- (9) Parto, K.; Azzam, S. I.; Banerjee, K.; Moody, G. Defect and 609 Strain Engineering of Monolayer WSe₂ Enables Site-Controlled 610 Single-Photon Emission up to 150 K. *Nat. Commun.* **2021**, *12* (1), 611 3585.
- (10) Branny, A.; Kumar, S.; Proux, R.; Gerardot, B. D. Deterministic 613 Strain-Induced Arrays of Quantum Emitters in a Two-Dimensional 614 Semiconductor. *Nat. Commun.* **2017**, *8*, 15053.
- (11) Grosso, G.; Moon, H.; Lienhard, B.; Ali, S.; Efetov, D. K.; 616 Furchi, M. M.; Jarillo-Herrero, P.; Ford, M. J.; Aharonovich, I.; 617 Englund, D. Tunable and High-Purity Room Temperature Single- 618 Photon Emission from Atomic Defects in Hexagonal Boron Nitride. 619 Nat. Commun. 2017, 8 (1), 705–713.
- (12) Branny, A.; Wang, G.; Kumar, S.; Robert, C.; Lassagne, B.; 621 Marie, X.; Gerardot, B. D.; Urbaszek, B. Discrete Quantum Dot like 622 Emitters in Monolayer MoSe₂: Spatial Mapping, Magneto-Optics, and 623 Charge Tuning. *Appl. Phys. Lett.* **2016**, 108 (14), 142101.

- 625 (13) Hus, S. M.; Ge, R.; Chen, P. A.; Liang, L.; Donnelly, G. E.; Ko, 626 W.; Huang, F.; Chiang, M. H.; Li, A. P.; Akinwande, D. Observation 627 of Single-Defect Memristor in an MoS₂ Atomic Sheet. *Nat.* 628 *Nanotechnol.* **2021**, *16* (1), 58–62.
- 629 (14) Chakraborty, C.; Kinnischtzke, L.; Goodfellow, K. M.; Beams, 630 R.; Vamivakas, A. N. Voltage-Controlled Quantum Light from an 631 Atomically Thin Semiconductor. *Nat. Nanotechnol.* **2015**, *10* (6), 632 507–511.
- 633 (15) Klein, J.; Lorke, M.; Florian, M.; Sigger, F.; Sigl, L.; Rey, S.; 634 Wierzbowski, J.; Cerne, J.; Müller, K.; Mitterreiter, E.; Zimmermann, 635 P.; Taniguchi, T.; Watanabe, K.; Wurstbauer, U.; Kaniber, M.; Knap, 636 M.; Schmidt, R.; Finley, J. J.; Holleitner, A. W. Site-Selectively 637 Generated Photon Emitters in Monolayer MoS₂ via Local Helium Ion 638 Irradiation. *Nat. Commun.* **2019**, *10* (1), 2755.
- 639 (16) Barthelmi, K.; Klein, J.; Hötger, A.; Sigl, L.; Sigger, F.; 640 Mitterreiter, E.; Rey, S.; Gyger, S.; Lorke, M.; Florian, M.; Jahnke, F.; 641 Taniguchi, T.; Watanabe, K.; Zwiller, V.; Jöns, K. D.; Wurstbauer, U.; 642 Kastl, C.; Weber-Bargioni, A.; Finley, J. J.; Müller, K.; Holleitner, A. 643 W. Atomistic Defects as Single-Photon Emitters in Atomically Thin 644 MoS₂. Appl. Phys. Lett. 2020, 117, 070501.
- 645 (17) Chakraborty, C.; Goodfellow, K. M.; Nick Vamivakas, A. 646 Localized Emission from Defects in MoSe₂ Layers. *Opt. Mater. Express* 647 **2016**, 6 (6), 2081–2087.
- 648 (18) Luo, Y.; Shepard, G. D.; Ardelean, J. V.; Rhodes, D. A.; Kim, B.; 649 Barmak, K.; Hone, J. C.; Strauf, S. Deterministic Coupling of Site-650 Controlled Quantum Emitters in Monolayer WSe₂ to Plasmonic 651 Nanocavities. *Nat. Nanotechnol.* **2018**, *13*, 1137–1142.
- 652 (19) Dang, J.; Sun, S.; Xie, X.; Yu, Y.; Peng, K.; Qian, C.; Wu, S.; 653 Song, F.; Yang, J.; Xiao, S.; Yang, L.; Wang, Y.; Rafiq, M. A.; Wang, 654 C.; Xu, X. Identifying Defect-Related Quantum Emitters in 655 Monolayer WSe₂. npj 2D Mater. Appl. 2020, 4 (1), 2.
- 656 (20) Schuler, B.; Cochrane, K. A.; Kastl, C.; Barnard, E. S.; Wong, 657 E.; Borys, N. J.; Schwartzberg, A. M.; Ogletree, D. F.; de Abajo, F. J. 658 G.; Weber-Bargioni, A. Electrically Driven Photon Emission from 659 Individual Atomic Defects in Monolayer WS ₂. *Sci. Adv.* **2020**, *6* (38), 660 1–7.
- 661 (21) Palacios-Berraquero, C.; Kara, D. M.; Montblanch, A. R.-P.; 662 Barbone, M.; Latawiec, P.; Yoon, D.; Ott, A. K.; Loncar, M.; Ferrari, 663 A. C.; Atatüre, M. Large-Scale Quantum-Emitter Arrays in Atomically 664 Thin Semiconductors. *Nat. Commun.* **2017**, *8*, 15093.
- 665 (22) Zhao, H.; Pettes, M. T.; Zheng, Y.; Htoon, H. Site-Controlled 666 Telecom-Wavelength Single-Photon Emitters in Atomically-Thin 667 MoTe₂. *Nat. Commun.* **2021**, *12* (1), 6753–6760.
- 668 (23) Shaik, A. B. D.; Palla, P. Optical Quantum Technologies with 669 Hexagonal Boron Nitride Single Photon Sources. *Sci. Rep.* **2021**, *11* 670 (1), 12285–12312.
- 671 (24) Tran, T. T.; Bray, K.; Ford, M. J.; Toth, M.; Aharonovich, I. 672 Quantum Emission from Hexagonal Boron Nitride Monolayers. *Nat.* 673 *Nanotechnol.* **2016**, *11* (1), 37–41.
- 674 (25) Tonndorf, P.; Del Pozo-Zamudio, O.; Gruhler, N.; Kern, J.; 675 Schmidt, R.; Dmitriev, A. I.; Bakhtinov, A. P.; Tartakovskii, A. I.; 676 Pernice, W.; Michaelis de Vasconcellos, S.; Bratschitsch, R. On-Chip 677 Waveguide Coupling of a Layered Semiconductor Single-Photon 678 Source. *Nano Lett.* 2017, 17 (9), 5446–5451.
- 679 (26) Tonndorf, P.; Schwarz, S.; Kern, J.; Niehues, I.; Del Pozo-680 Zamudio, O.; Dmitriev, A. I.; Bakhtinov, A. P.; Borisenko, D. N.; 681 Kolesnikov, N. N.; Tartakovskii, A. I.; Michaelis de Vasconcellos, S.; 682 Bratschitsch, R. Single-Photon Emitters in GaSe. 2d Mater. 2017, 4 683 (2), 021010.
- 684 (27) Tran, T. T.; Choi, S.; Scott, J. A.; Xu, Z.; Zheng, C.; Seniutinas, 685 G.; Bendavid, A.; Fuhrer, M. S.; Toth, M.; Aharonovich, I. Room-686 Temperature Single-Photon Emission from Oxidized Tungsten 687 Disulfide Multilayers. *Adv. Opt. Mater.* **2017**, *5* (5), 1600939.
- 688 (28) Wang, W.; Jones, L. O.; Chen, J. S.; Schatz, G. C.; Ma, X. 689 Utilizing Ultraviolet Photons to Generate Single-Photon Emitters in 690 Semiconductor Monolayers. *ACS Nano* **2022**, *16* (12), 21240–21247. 691 (29) Lin, Y.; Hathaway, E.; Habis, F.; Wang, Y.; Rodriguez, R. G.; 692 Alnasser, K.; Hurley, N.; Cui, J. Enhanced Emission from Defect 693 Levels in Multilayer MoS₂. *Adv. Opt. Mater.* **2022**, *10* (19), 2201059.

- (30) Tran Khac, B. C.; Jeon, K.-J.; Choi, S. T.; Kim, Y. S.; DelRio, F. 694 W.; Chung, K.-H. Laser-Induced Particle Adsorption on Atomically 695 Thin MoS₂. ACS Appl. Mater. Interfaces **2016**, 8 (5), 2974–2984.
- (31) Castellanos-Gomez, A.; Barkelid, M.; Goossens, A. M.; Calado, 697 V. E.; van der Zant, H. S. J.; Steele, G. A. Laser-Thinning of MoS 2: 698 On Demand Generation of a Single-Layer Semiconductor. *Nano Lett.* 699 **2012**, 12 (6), 3187–3192.
- (32) Tran-Khac, B.-C.; White, R. M.; DelRio, F. W.; Chung, K.-H. 701 Layer-by-Layer Thinning of MoS $_2$ via Laser Irradiation. Nano- 702 technology 2019, 30 (27), 275302.
- (33) Alrasheed, A.; Gorham, J. M.; Tran Khac, B. C.; Alsaffar, F.; 704 DelRio, F. W.; Chung, K.-H.; Amer, M. R. Surface Properties of Laser-705 Treated Molybdenum Disulfide Nanosheets for Optoelectronic 706 Applications. ACS Appl. Mater. Interfaces 2018, 10 (21), 18104—707 18112.
- (34) Mitterreiter, E.; Schuler, B.; Micevic, A.; Hernangómez-Pérez, 709 D.; Barthelmi, K.; Cochrane, K. A.; Kiemle, J.; Sigger, F.; Klein, J.; 710 Wong, E.; Barnard, E. S.; Watanabe, K.; Taniguchi, T.; Lorke, M.; 711 Jahnke, F.; Finley, J. J.; Schwartzberg, A. M.; Qiu, D. Y.; Refaely- 712 Abramson, S.; Holleitner, A. W.; Weber-Bargioni, A.; Kastl, C. The 713 Role of Chalcogen Vacancies for Atomic Defect Emission in MoS₂. 714 Nat. Commun. 2021, 12 (1), 3822.
- (35) Sensoy, M. G.; Vinichenko, D.; Chen, W.; Friend, C. M.; 716 Kaxiras, E. Strain Effects on the Behavior of Isolated and Paired Sulfur 717 Vacancy Defects in Monolayer MoS₂. *Phys. Rev. B* **2017**, 95 (1), 718 014106.
- (36) Lin, Y.; Hurley, N.; Kamau, S.; Hathaway, E.; Jiang, Y.; 720 Rodriguez, R. G.; Varghese, S.; Krylyuk, S.; Davydov, A. V.; Wang, Y.; 721 Kaul, A.; Cui, J. Strain-Activated Stimulated Emission from Multilayer 722 MoSe 2 in a Narrow Operation Window. *Phys. Status Solidi RRL* **2024**, 723 18 (2), 1–8.
- (37) Dutta, N. K.; Craft, D. C. Effect of Stress on the Polarization of 725 Stimulated Emission from Injection Lasers. *J. Appl. Phys.* **1984**, 56 726 (1), 65–70.
- (38) Hurley, N.; Bhandari, B.; Kamau, S.; Gonzalez Rodriguez, R.; 728 Squires, B.; Kaul, A. B.; Cui, J.; Lin, Y. Selective CW Laser Synthesis 729 of MoS2 and Mixture of MoS2 and MoO2 from (NH4)2MoS4 Film. 730 Micromachines 2024, 15 (2), 258.
- (39) Wei, Y.; Liu, S.; Li, X.; Yu, Y.; Su, X.; Li, S.; Shang, X.; Liu, H.; 732 Hao, H.; Ni, H.; Yu, S.; Niu, Z.; Iles-Smith, J.; Liu, J.; Wang, X. 733 Tailoring Solid-State Single-Photon Sources with Stimulated 734 Emissions. *Nat. Nanotechnol.* **2022**, *17* (5), 470–476.
- (40) Hong, J.; Hu, Z.; Probert, M.; Li, K.; Lv, D.; Yang, X.; Gu, L.; 736 Mao, N.; Feng, Q.; Xie, L.; Zhang, J.; Wu, D.; Zhang, Z.; Jin, C.; Ji, 737 W.; Zhang, X.; Yuan, J.; Zhang, Z. Exploring Atomic Defects in 738 Molybdenum Disulphide Monolayers. *Nat. Commun.* **2015**, *6* (1), 739 6293.